

# ***Low-voltage 2D materials-based printed field-effect transistors for integrated digital and analog electronics on paper***

Silvia Conti<sup>1\*</sup>, Lorenzo Pimpolari<sup>1\*</sup>, Gabriele Calabrese<sup>1</sup>, Robyn Worsley<sup>2</sup>, Subimal Majee<sup>2</sup>, Dmitry K. Polyushkin<sup>3</sup>, Matthias Paur<sup>3</sup>, Simona Pace<sup>4</sup>, Dong Hoon Keum<sup>4</sup>, Filippo Fabbri<sup>4</sup>, Giuseppe Iannaccone<sup>1</sup>, Massimo Macucci<sup>1</sup>, Camilla Coletti<sup>4</sup>, Thomas Mueller<sup>3</sup>, Cinzia Casiraghi<sup>2</sup>, Gianluca Fiori<sup>1</sup>

<sup>1</sup>*Dipartimento di Ingegneria dell'Informazione, University of Pisa, Pisa, Italy*

<sup>2</sup>*Department of Chemistry, University of Manchester, Manchester, UK*

<sup>3</sup>*Institute for Microelectronics (TU Wien), Vienna, Austria*

<sup>4</sup>*Center for Nanotechnology Innovation (NEST), Pisa, Italy*

*\*These two authors contributed equally*

**Paper is the ideal substrate for the development of flexible and environmentally sustainable ubiquitous electronic systems, enabling new applications in the context of the Internet of Things (IoTs). Two-dimensional materials have outstanding electronic and optical properties, and they are compatible with flexible substrates. Besides, combining different 2D materials enables to design a large variety of devices, which could be exploited in many IoTs applications, ranging from wearable electronics to smart packaging.**

**In this work, we demonstrate high-performance MoS<sub>2</sub> field-effect transistors on paper substrates fabricated with a new “channel-array” approach, which combines the advantages of chemical vapor deposition (CVD) and inkjet-printing as fabrication techniques. This method is based on the preparation of a channel array, i.e. the pre-**

**deposition on paper of a pattern of CVD-grown MoS<sub>2</sub> to be used as channels. Inkjet printing is then used to complete transistors and circuits fabrication, through the deposition of dielectric layers, contacts, and connections. We show that the channel-array approach allows the fabrication of 2D materials-based transistors on paper with excellent current modulation ( $I_{ON}/I_{OFF}$  up to  $10^5$ ) and mobility (up to  $15 \text{ cm}^2 \text{ V}^{-1} \text{ s}^{-1}$ ). Fully functional integrated circuits of digital and analog building blocks, such as high-gain inverters, logic gates, and current mirrors are demonstrated, confirming the potential of this approach for ubiquitous electronics on paper.**

In recent years, electronics has witnessed impressive technological achievements, due to the development of new processes and materials with extraordinary electrical and mechanical properties, which have enabled the development of Internet of Things (IoTs) applications, ranging from wearable electronics to mobile healthcare. This has led to a continuous and dramatic increase in demand of light-weight, flexible, and low-cost devices, posing strong constraints on the traditional fabrication methods <sup>1,2</sup>. In addition, this type of pervasive and versatile electronics had led to further concerns on sustainability, such as the treatment of waste at the end of the product life-cycle. Derived from abundant and renewable raw materials, paper-based consumer electronics is expected to alleviate landfill and environmental problems and to reduce the impact associated with recycling operations, whilst offering cost-effectiveness and large flexibility <sup>3</sup>. However, paper is a challenging substrate for electronics due to its high roughness and limiting processing temperature and the lack of a winning fabrication technique is preventing its exploitation at the industrial level.

Two-dimensional materials (2DMs) combine excellent tunable electronic properties with high mechanical flexibility, making them extremely promising as building blocks for flexible electronics <sup>4,5</sup>. Moreover, they can be easily produced in solution with mass scalable and low-

cost techniques, such as liquid-phase exfoliation (LPE) <sup>6</sup>, enabling their deposition by simple fabrication techniques such as inkjet printing <sup>7,8,9,10,11</sup>. 2D semiconducting materials, such as transition metal dichalcogenides (TMDCs) <sup>12</sup>, with extended bandgap tunability through composition, thickness, and possibly even strain control, represent promising materials as channels for thin film transistors (TFTs), which are fundamental components in electronics. However, up to now, fully printed TMDCs based transistors have demonstrated limited performance, showing mobility of the order of under  $0.5 \text{ cm}^2 \text{ V}^{-1} \text{ s}^{-1}$  and  $I_{ON}/I_{OFF}$  ratios of hundreds, using liquid electrolytes as insulating layers <sup>13,14</sup>. Among the various TMDCs, molybdenum disulfide ( $\text{MoS}_2$ ) has been widely studied, due to its outstanding electrical and optical properties <sup>15,16,17,18</sup>. Lin *et al.* <sup>19</sup> reported a TFT made with solution-processed  $\text{MoS}_2$ , showing remarkable performance (average mobility of around  $7\text{--}11 \text{ cm}^2 \text{ V}^{-1} \text{ s}^{-1}$ ), but device fabrication required acid cleaning and annealing above  $200 \text{ }^\circ\text{C}$ , which are incompatible with substrates such as paper. A large mobility of  $19 \text{ cm}^2 \text{ V}^{-1} \text{ s}^{-1}$  for a  $\text{MoS}_2$ /graphene transistor was reported in reference <sup>20</sup>: graphene allows increasing carrier mobility, but this negatively affects the  $I_{ON}/I_{OFF}$  ratio.

We propose a new fabrication technique that combine the use of high mobility  $\text{MoS}_2$  channels grown by CVD and inkjet-printing technique for the fabrication of transistors and circuits, exploiting 2DMs-based inks, whose capability to be printed on top of CVD grown materials has been successfully demonstrated in <sup>10</sup>. This approach is called “channel array”, as it is based on the deposition of several channels on a customized substrate, onto which the rest of the device and circuit is fabricated. The “channel array” technique consists of two steps: first, the channel array is fabricated by transferring on the paper substrate stripes of CVD grown  $\text{MoS}_2$ , which will be used as transistors channels. In the second step, the field effect transistor (FET) and the rest of the circuit are fabricated by customizing the channel array by inkjet-printing the source and drain contacts (i.e., channel length and width), gate dielectric, gate contacts, and all

connections. This approach allows to keep the flexibility and versatility of an all-inkjet technology, with the difference that here a high-quality channel is already placed on the substrate, by taking advantage of the CVD grown TMDC.

The MoS<sub>2</sub> field effect transistors fabricated with the channel array method operate at supply voltage below 2 V, with remarkable transistor performance, such as an average field effect mobility of 5.9 cm<sup>2</sup> V<sup>-1</sup> s<sup>-1</sup> (up to 15 cm<sup>2</sup> V<sup>-1</sup> s<sup>-1</sup>), negligible leakage currents (smaller than 1 nA), and  $I_{ON}/I_{OFF}$  ratios of up to 10<sup>5</sup>, which have never been recorded on paper. We further exploit the possibility to produce high performance transistors with the channel array method by demonstrating more complex circuits, such as logic gates (such as NOT and NAND) and analog circuits. This paves the way towards the application of the channel array approach in all applications where flexible and/or disposable electronics are required.

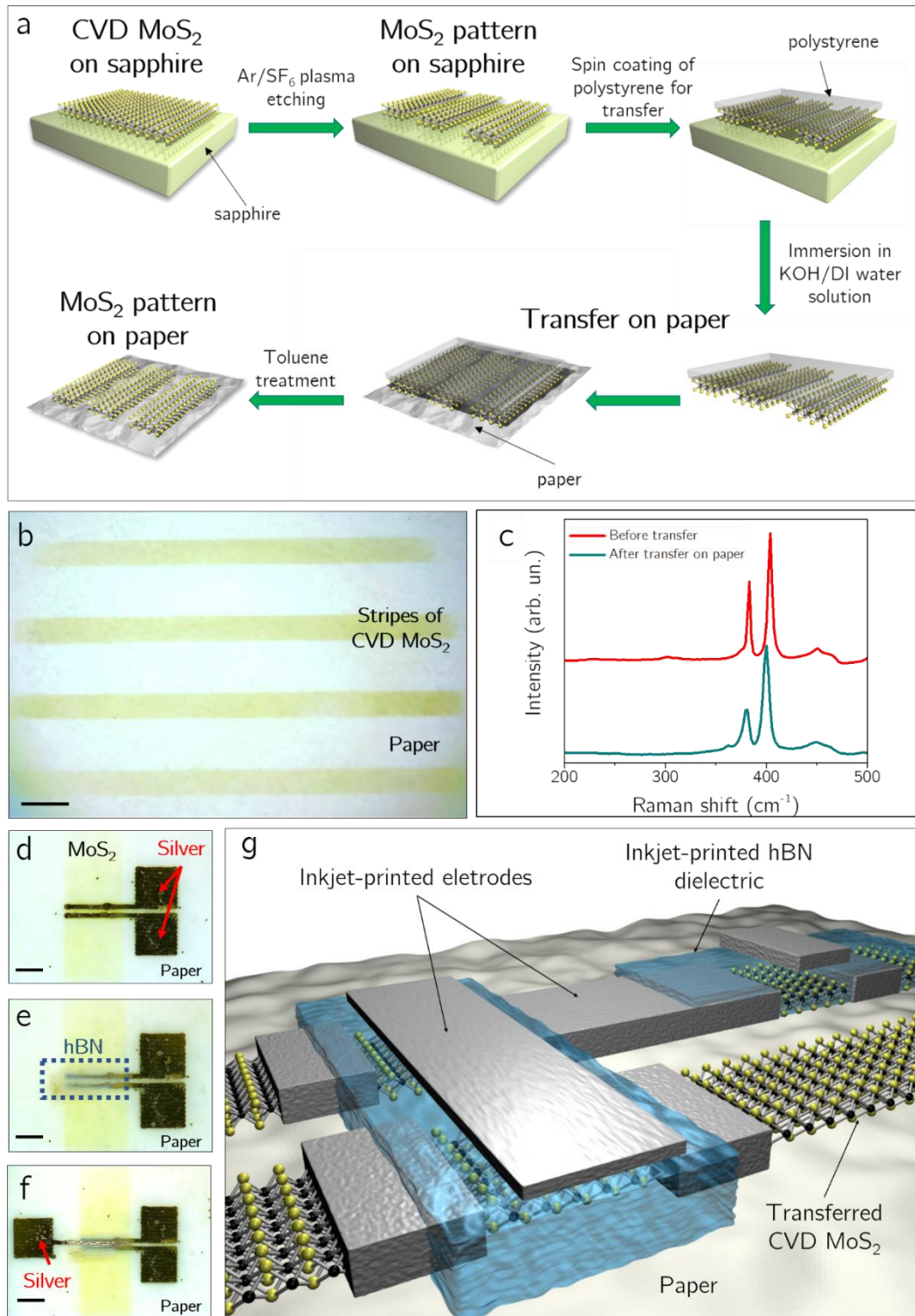
### **Fabrication of MoS<sub>2</sub> FETs on paper**

Figure 1a illustrates the procedure followed to pattern CVD MoS<sub>2</sub> and its transfer to paper substrate (a detailed description of the procedure is reported in *Methods*, an alternative method for CVD growth and transfer is presented in *Section S4* of the *Supplementary Information*). After the transfer, the polystyrene carrier film is dissolved in toluene, resulting in MoS<sub>2</sub> stripes on a paper substrate, as shown in Figure 1b.

To evaluate the crystalline quality of the MoS<sub>2</sub> before and after the transfer process from the rigid substrate to the paper, Raman spectroscopy is employed. Figure 1c shows the Raman spectra before (red line) and after (cyan line) the transfer. The red spectrum presents the E<sub>2g</sub> and A<sub>1g</sub> modes at 383 cm<sup>-1</sup> and at 403 cm<sup>-1</sup> of single-layer MoS<sub>2</sub>, representative of the in-plane and out-of-plane vibrations of S–Mo–S, respectively<sup>21</sup>. After the transfer process, the MoS<sub>2</sub> Raman modes appear slightly shifted and broadened, i.e. the E<sub>2g</sub> and A<sub>1g</sub> modes peak at 380 cm<sup>-1</sup> and at 400 cm<sup>-1</sup>, respectively. As previously reported in<sup>22</sup>, the softening of Raman modes can be attributed to uniaxial strain, albeit the E<sub>2g</sub> mode should suffer a larger shift compared to

the  $A_{1g}$  mode. In our case, the softening of the Raman modes is comparable, ruling out any strain effect on the  $MoS_2$ . Therefore, we argue that the softening is mainly due to heating effects related to the poor heat dissipation of the paper substrate. This hypothesis is also supported by the broadening of the full-width-at-half-maximum (FWHM) of both modes. Indeed, the  $E_{2g}$  FWHM increases from  $\sim 3\text{ cm}^{-1}$ , before transfer, up to  $\sim 7\text{ cm}^{-1}$  after the transfer process. In the case of the  $A_{1g}$  mode the broadening is less evident, with the FWHM increasing from  $\sim 4\text{ cm}^{-1}$  up to  $\sim 6\text{ cm}^{-1}$ .

Figure 1d-f show the fabrication of inkjet-printed  $MoS_2$  FETs on paper. Inkjet-printing was chosen as the fabrication technique for a fast prototyping, since it is a versatile, additive, mask-less, low-material, low-time, and low-power consuming approach<sup>23</sup>. First, the source and drain contacts are printed on a  $MoS_2$  stripe to define the channel area of the transistor (Figure 1d). Secondly, a hBN film is printed on the  $MoS_2$  channel (Figure 1e) due to its excellent dielectric properties and negligible leakage currents<sup>9,13,24,25</sup>. Finally, a top gate electrode is printed on top of hBN (Figure 1f). Either silver or graphene inks have been used to print the source and drain contacts as well as the top gate contact. The FETs are then connected to each other using the routes defined between  $MoS_2$  stripes, to create the integrated circuit in an efficient and versatile way. This approach is qualitatively described in Figure 1g.



**Figure 1 | Transferring scheme of MoS<sub>2</sub> channel stripes and fabrication process of MoS<sub>2</sub> FETs. a,** Schematic representation of the patterning and transferring procedure employed to obtain MoS<sub>2</sub> stripes on paper. **b,** Optical micrograph showing the transferred MoS<sub>2</sub> stripes on paper. The scale bar corresponds to 1 mm. **c,** Raman spectra acquired on the as-grown MoS<sub>2</sub> layer on rigid substrate (red line) and after MoS<sub>2</sub> transfer to paper (cyan line). **d-f.** Fabrication steps of the inkjet-printed transistors on paper: **d,** inkjet-printing of silver source and drain contacts. **e,** inkjet-printing of the h-BN dielectric layer (defined by the blue-dotted frame). **f,** inkjet-printing of silver top gate contact. The scale bars in d-f correspond to 250 μm. **g,** Sketch showing an inkjet-printed circuit on paper with CVD-grown MoS<sub>2</sub> channel.

## Electrical characterization of MoS<sub>2</sub> FETs

At first, a commercial silver ink (see *Methods*) was chosen to print the electrodes, because it can assure very high conductivity with just one printing pass, and it has shown ohmic contact with MoS<sub>2</sub><sup>26</sup>. Typical transfer and output characteristics of the MoS<sub>2</sub> FETs are reported in Figure 2a and Figure 2c. The devices work in the enhancement mode, can operate at low supply voltage (< 2 V), and exhibit a threshold voltage ( $V_{TH}$ ) ranging between 0.0 V and 1.0 V (see Figure S3c, *Supplementary Information*). As can be seen, the leakage current  $I_{GS}$  (red dots, Figure 2a) through the insulator is negligible as compared to the drain current  $I_{DS}$  (black dots, logarithmic scale, Figure 2a; black dots, linear scale, Figure 2b), further confirming the good insulating properties of the inkjet-printed hBN film. The saturation regime is reached for low drain-to-source voltage ( $V_{DS}$ ), i.e.,  $V_{DS} < 2$  V. Almost negligible contact resistance is shown from the output characteristic. Indeed, as can be seen from the log-log plot (Figure 2d), the linearity parameter  $\gamma$ , describing the relation  $I_{DS} \propto V_{DS}^\gamma$ , is found to be 1.1 on average, indicating a good contact between the CVD MoS<sub>2</sub> and the silver inkjet-printed electrodes.

Charge carrier field-effect mobility ( $\mu_{FE}$ ) is one of the most important figures of merit defining the quality of a transistor electrical performance. It can be extrapolated using the classical model for devices operating in the saturation regime ( $V_{DS} > V_{GS} - V_{TH}$ ):

$$\mu_{FE} = 2 \frac{L}{W} \frac{1}{C_i} \left( \frac{\partial \sqrt{I_{DS}}}{\partial V_{GS}} \right)^2 \quad (1)$$

where  $C_i$  is the capacitance of the insulator per unit area,  $W$  and  $L$  are the transistor channel width and length, respectively, and  $V_{GS}$  is the gate voltage. As suggested in reference<sup>27</sup>, in order to avoid any mobility overestimation, the capacitance has been measured in the quasi-static conditions (details about the quasi-static capacitance measurement and setup are reported in *Section 1* of the *Supplementary Information*). To this purpose, parallel plate capacitor structures, in which hBN is sandwiched between silver bottom/top electrodes were fabricated

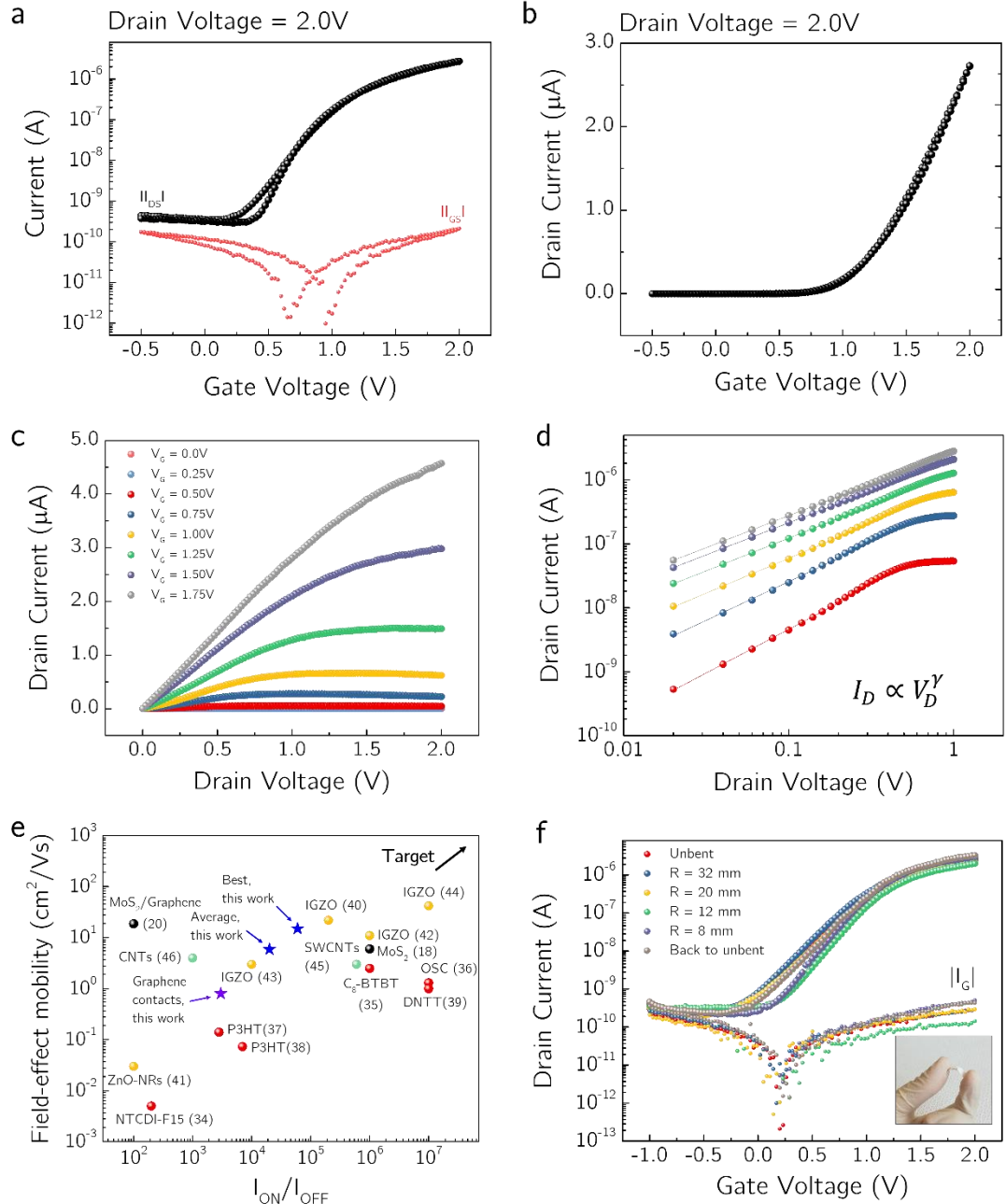
and tested (see *Methods*). The extracted average value of 230 nF/cm<sup>2</sup> is in line with other quasi-static measurement performed on both organic and hybrid materials<sup>27,28,29,30</sup>. Thanks to the high capacitive coupling, which results in an enhanced polarization and leads to a high number of carriers at the insulator-semiconductor interface, the devices show an average charge carrier mobility of 5.9 cm<sup>2</sup> V<sup>-1</sup> s<sup>-1</sup> and  $I_{ON}/I_{OFF}$  ratio of 1.4x10<sup>4</sup> are obtained, where  $I_{ON}$  is defined as the  $I_{DS}$  measured when  $V_{DS}$  is equal to  $V_{GS}$  ( $V_{GS} = V_{DS} = 2V$ ), while  $I_{OFF}$  is the average  $I_{DS}$  in the subthreshold region ( $V_{GS} < V_{TH}$ ). The detailed electrical characterization is reported in Figure S2 and Figure S3. Remarkably, this mobility value is comparable to already reported CVD-grown MoS<sub>2</sub> transistors fabricated on rigid substrates using standard microelectronic fabrication techniques<sup>31,32,33</sup>, confirming that our methodology, based on the channel array, allows to use inkjet-printing for the fabrication of the devices, without affecting the electronic properties of the channel.

Figure 2e shows  $\mu_{FE}$  and  $I_{ON}/I_{OFF}$  for our devices compared with those previously reported in the literature: the closer the points to the top-right corner, the better the performance. We considered only transistors fully fabricated on paper or transferred on paper after fabrication. They have been divided into four groups according to the nature of the semiconductor used as channel: organic semiconductors<sup>34,35,36,37,38,39</sup>, inorganic oxide semiconductors<sup>40,41,42,43,44</sup>, carbon nanotubes<sup>45,46</sup> (CNTs), and 2D materials<sup>18,20</sup>. Notably, our devices are the only one, where the contacts and the insulating layer are deposited by means of inkjet-printing (for a detailed comparison see Table S1 in *Supplementary Information*). While maintaining a high  $I_{ON}/I_{OFF}$  ratio, the mobility values extracted from the MoS<sub>2</sub> FETs are larger than those obtained for organic semiconductors. It is worth mentioning, that the mobility extracted in this work is comparable to the one found in MoS<sub>2</sub> FETs fabricated using conventional microelectronic techniques<sup>18</sup>. Although there are transistors, as reported in references<sup>18,40,42,44</sup>, that show comparable or better performance than ours, we remark that, in those cases, expensive, and



time-consuming fabrication techniques were employed for their fabrication. Furthermore, many of these devices operate at moderate or large voltages ( $>10$  V), which is a crucial problem for portable applications, where low power consumption is often required.

In order to confirm the compatibility of our technology with flexible substrates, the electromechanical properties of the devices are investigated for various bending radii ( $R$ ). Figure 2f shows transfer characteristics recorded for  $R$  values of 32 mm, 20 mm, 12 mm, and 8 mm. No relevant changes both in the drain and the gate currents are observed, indicating that the device electrical performance is not affected under strain.



**Figure 2 | Electrical characterization of the MoS<sub>2</sub> FETs with inkjet-printed silver contacts in ambient conditions.** Typical transfer characteristic curve measured as a function of the gate voltage for a drain voltage of 2.0 V. Logarithmic scale: black dots, drain current; red dots, gate current. **b**, Typical transfer characteristic curve measured as a function of the gate voltage for a drain voltage of 2.0 V in linear scale. **c**, Typical output characteristic measured at different gate voltages (from  $V_{GS} = 0.0$  V to  $V_{GS} = 1.75$  V, steps of 0.25 V). **d**, Log-log curves of the output characteristic in low drain voltage region. Ohmic behavior is observed, suggesting good electrical contact between the silver contacts and MoS<sub>2</sub>. **e**, Field-effect mobility and  $I_{ON}/I_{OFF}$  ratio for TFTs on flexible substrates previously reported in the literature. Blue stars, this work, inkjet-printed silver contacts; purple star, this work, inkjet-printed graphene contacts; red dots, organic semiconductors (ref 34-39); yellow dots, inorganic oxides (40-44); green dots, CNTs (45,46); black dots, 2D materials (18,20). **f**, Transfer characteristics and gate leakage currents measured for different bending radii along the current direction for a drain voltage of 2 V; inset, picture of a sample with MoS<sub>2</sub> FET fabricated on paper.

We have then focused on the fabrication of a fully 2D-material-based transistors with inkjet-printed graphene source, drain, and gate contacts (see *Methods*). An optical micrograph of a fully 2D-material-based FET is shown in Figure 3a, whilst Figure 3b and Figure 3c report typical transfer and output characteristic, respectively. These transistors show a reduced effective  $\mu_{FE}$  ( $\sim 0.8 \text{ cm}^2 \text{ V}^{-1} \text{ s}^{-1}$ ), and an  $I_{ON}/I_{OFF}$  ratio about one order of magnitude smaller ( $\sim 3 \times 10^3$ ), compared to transistors with silver contacts (Figure 2e). The reduced performance is likely related to the formation of Schottky contacts, which in turn increases the contact resistance, as evident from Figure 3c, where non-linear behavior of the output characteristic can be observed for small  $V_{DS}$ . This behavior typical of FETs with Schottky barrier contacts. However, it is remarkable that the extracted field-effect mobility is only one order of magnitude smaller than the one obtained for a thin film transistor with exfoliated  $\text{MoS}_2$  channel and CVD-grown graphene source/drain electrodes ( $4.5 \text{ cm}^2 \text{ V}^{-1} \text{ s}^{-1}$ )<sup>47</sup>.

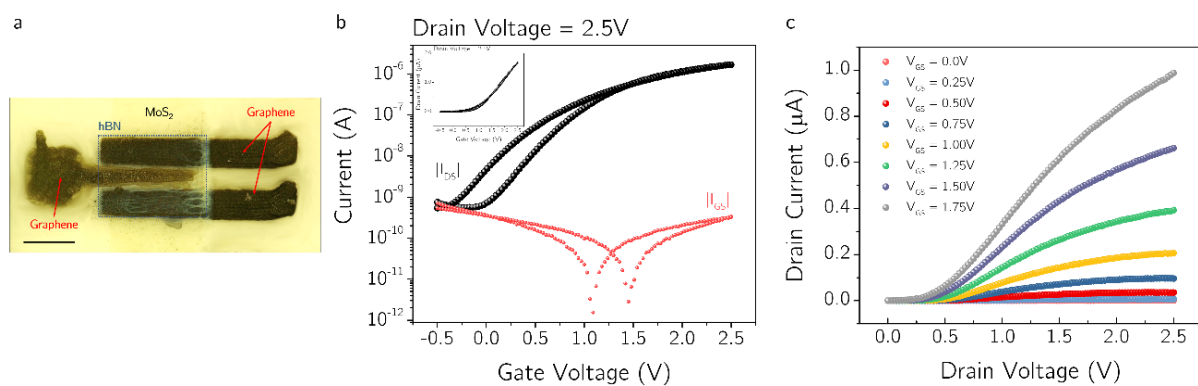


**Figure 3 | Optical image and electrical characterization of a fully 2D-material-based FETs.** **a**, Optical micrograph of a fully 2D-material-based transistor on paper. The scale bar corresponds to  $250 \mu\text{m}$ . **b**, Typical transfer characteristic curve measured as a function of the gate voltage for a drain voltage of  $2.5 \text{ V}$ . Logarithmic scale: black dots, drain current; red dots, gate current. inset, Typical transfer characteristic curve measured as a function of the gate voltage for a drain voltage of  $2.5 \text{ V}$  in linear scale. **c**, Typical output characteristic curves measured at increasing gate voltages (from  $V_{GS} = 0.0 \text{ V}$  to  $V_{GS} = 1.75 \text{ V}$ , steps of  $0.25 \text{ V}$ ).

## Integrated circuits on paper

To demonstrate the potential of the fabricated FETs as building blocks for integrated circuits exploiting the channel array technology, different types of circuits have been designed and fabricated.  $\text{MoS}_2$  FETs with inkjet-printed silver contacts were selected due to the high  $I_{ON}/I_{OFF}$

ratio, intrinsic gain, and low power supply voltage to fabricate a resistor-transistor logic (RTL) inverter, consisting of a transistor and an inkjet-printed graphene resistor. Figure 4a and Figure 4b show the schematic and the optical image of a RTL inverter, respectively. The transfer characteristic of an inverter is shown in Figure 4c (left axis), together with the gain  $G$  (right axis), defined as the slope  $dV_{OUT}/dV_{IN}$  of the transfer curve (where  $V_{IN}$  and  $V_{OUT}$  are the input and output voltages, respectively). The inverter exhibits a high gain value, close to 30 under a voltage bias of 5 V, in agreement with previously reported inverters based on CVD-grown MoS<sub>2</sub> fabricated on rigid substrates<sup>32,48</sup>.

The schematic and the optical image of a NAND gate are shown in Figure 4d and Figure 4e, while Figure 4f shows the output voltage of the circuit as a function of the inputs ( $V_{IN1}, V_{IN2}$ ). The low and high logic values of the inputs correspond to voltages of 0 V and 5 V, respectively. The output voltage is high (i.e. at logic state “1”) when at least one input is in the logic state “0”, and therefore at least one transistor is in the OFF state. The output voltage is low (i.e. at logic state “0”) only when both inputs are at the logic state “1”: in these conditions both transistors are in the ON state. The possibility to implement NAND gates is particularly important, since all other logic functions can be implemented using NAND gates.

As a further demonstration of the potential of the presented technology, we propose an application for analog electronics. Current mirrors are fundamental building blocks in analog electronic circuits, where they are widely used for operational amplifiers, bandgap voltage reference, etc.<sup>49</sup>, and they can also be exploited in neural networks, in order to implement matrix-vector multiplication<sup>50</sup>. Figure 4g and Figure 4h show the schematic and the optical image of the fabricated current mirror. The output transistor ( $M_2$ ) is 10 times wider than the input transistor ( $M_1$ ), while all the other transistor parameters are identical; therefore, the current mirror has a nominal gain of 10. Figure 4i shows the current mirror output characteristic, i.e., the output current as a function of the output voltage, for two different values

of the input reference current. As shown in the plot, for sufficiently high output voltages (i.e.,  $M_2$  in saturation) the output current is about 10 times larger than the reference current ( $I_{REF}$ ), in accordance with the circuit design.

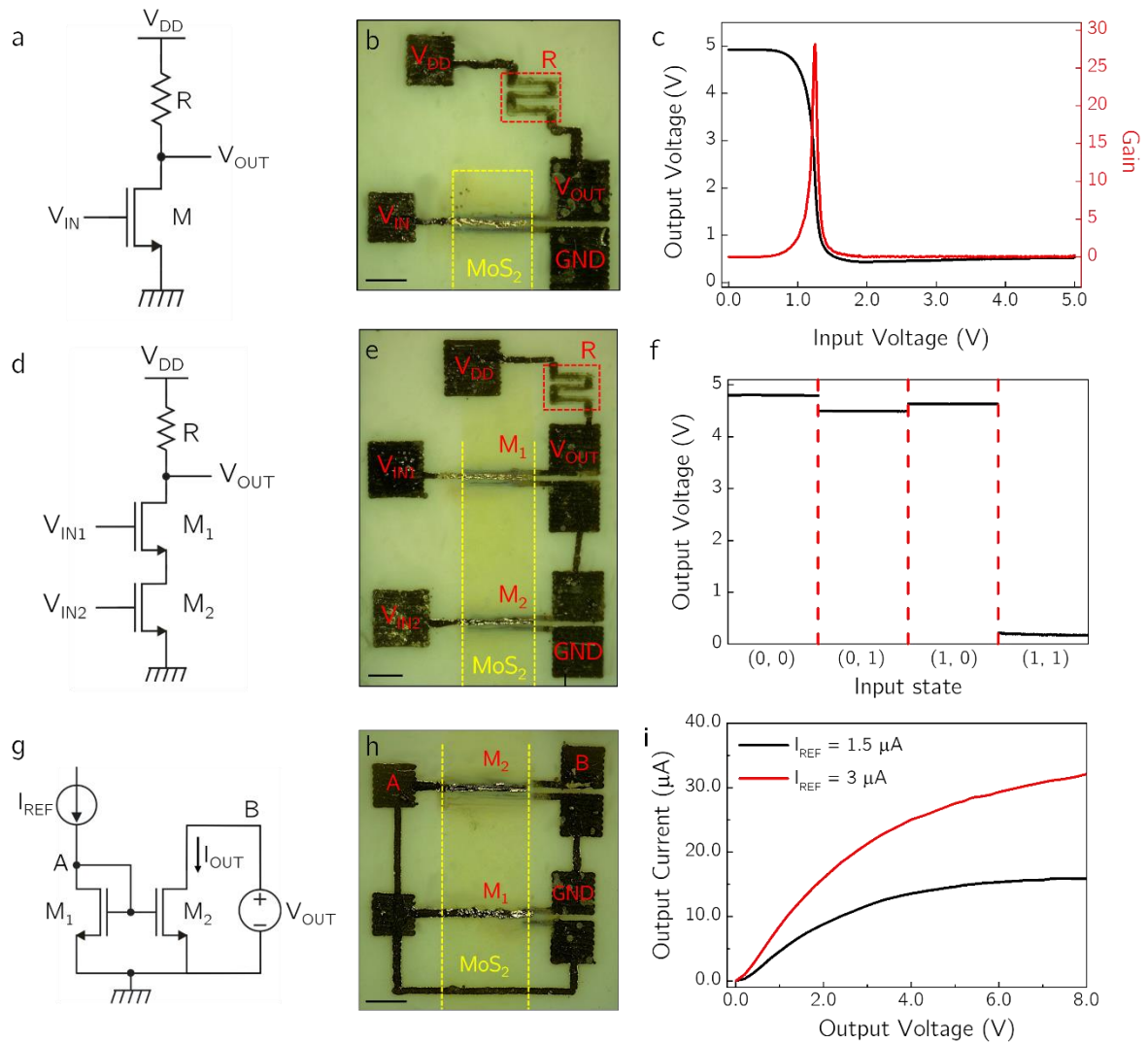


**Figure 4 | Logic gates and current mirror based on inkjet-printed  $\text{MoS}_2$  FETs. a, d, g and b, e, h** Electrical schematics and optical images of an inverter (a, b), a NAND gate (d, e) and a current mirror (g, h).  $V_{DD}$ , supply voltage;  $GND$ , ground reference;  $V_{IN}$  and  $V_{OUT}$ , input and output voltage;  $M$ , inkjet-printed transistor.  $R$ , inkjet-printed graphene resistor. The scale bars in b, e, h correspond to  $250 \mu\text{m}$ . **c**, Output voltage (left axis) and voltage gain (right axis) of the inverter gate as a function of the input voltage. **f**, Output voltage of the NAND gate as a function of the input states ( $V_{IN1}$ ,  $V_{IN2}$ ). Voltage bias is 5 V for both the inverter and the NAND gate. **i**, Output current of the current mirror as a function of the output voltage for two different values of the reference current.

## Conclusions

We have successfully demonstrated high performance  $\text{MoS}_2$  based transistors that combine the numerous advantages of using paper as a substrate with the versatility of inkjet-printing

technique, whilst maintaining the electrical properties of CVD-grown MoS<sub>2</sub>. A maximum field-effect mobility of 15 cm<sup>2</sup> V<sup>-1</sup> s<sup>-1</sup> and an  $I_{ON}/I_{OFF}$  ratio of up to 10<sup>5</sup> were achieved. Bending tests have shown that the device electrical properties are robust under applied strain (up to curvature radius of 8 mm). Moreover, our device fabrication approach has been proven to be suitable for the development of complete integrated circuits, such as high-gain inverters, logic gates, and current mirrors. This work demonstrates the great potential of the channel array technology for next-generation electronics on paper, ranging from analogic to digital circuits for cost-efficient and practical applications.

## Methods

### Materials

PEL P60 (purchased from Printed Electronics Limited) is used as paper substrate. A commercial silver ink (Sigma Aldrich) is used to print the metal contacts. Bulk graphite (purchased from Graphexel or Sigma-Aldrich, 99.5% grade) and bulk boron nitride (purchased from Sigma-Aldrich, >1 μm, 98% grade) powders were used to prepare the 2DMs inks. The bulk powders are dispersed in deionized water (resistivity 18.2 MΩ cm<sup>-1</sup>) at a concentration of 3 mg mL<sup>-1</sup> and 1-pyrenesulphonic acid sodium salt (PS1, purchased from Sigma-Aldrich), purity ≥ 97%, is added at a concentration of 1 mg mL<sup>-1</sup>. The graphite and boron nitride dispersions are then sonicated for 72 h and 120 h respectively using a 300 W Hilsonic HS 1900/Hilsonic FMG 600 bath sonicator at 20 °C. The resultant dispersions is centrifuged at 3500 rpm (g factor = 903) for 20 minutes at 20 °C using a Sigma 1-14K refrigerated centrifuge in order to separate out and discard the residual bulk, non-exfoliated flakes. The remaining supernatant, now containing the correct flake size and monolayer percentage, is centrifuged twice to remove excess PS1 from the dispersion. After washing, the precipitate is re-dispersed in the printing solvent, made as described in <sup>10</sup>. The concentration of the resultant inks are assessed using a Varian Cary 5000 UV-Vis spectrometer and the Lambert-Beer law, with

extinction coefficients of 2460 (at 660 nm) and 1000 L g<sup>-1</sup> m<sup>-1</sup> (at 550 nm) for graphene<sup>6</sup> and hBN<sup>51</sup>, respectively. Full characterization of the material (lateral size and thickness distribution, crystallinity, etc.) has been presented in references<sup>10,24</sup>.

### **Growth of MoS<sub>2</sub> and transfer on paper**

Single- and few-layer MoS<sub>2</sub> have been grown by Chemical Vapour Deposition (CVD) on c-plane sapphire as described in reference<sup>52</sup>. CVD growth is performed at atmospheric pressure using ultra-high-purity argon as the carrier gas. The substrates are placed face-down 15 mm above a crucible containing ~3 mg of MoO<sub>3</sub> (99.998% Alfa Aesar) and loaded into a split-tube two-zone CVD furnace with a 30 mm outer diameter quartz tube. A second crucible containing 1 g of sulphur (99.9% purity, Sigma-Aldrich) is loaded upstream from the growth substrates and heated to 140°C. Just before starting the growth, the tube is flushed with Ar at room temperature and atmospheric pressure. The furnace is pre-heated to 750°C for few hours for temperature stabilization. The substrate and MoO<sub>3</sub> precursor were then loaded into the growth area of the furnace to start the growth. Ar is supplied with a flow of 10 sscm. After 10 min growth at 750 °C, the furnace is left to cool naturally. The synthesized MoS<sub>2</sub> film is transferred from the native sapphire substrate to the paper substrates<sup>53</sup>. Prior to the film transfer, MoS<sub>2</sub> is patterned to obtain a stripped structure on the growth substrate. The pattern is defined by means of Ar/SF<sub>6</sub> plasma etching in an Oxford Cobra Reactive Ion Etching system. The etch mask is created by optical lithography using AZ 5214E photoresist. A 5% KOH solution in DI water is employed to remove the etch mask. The sample is then rinsed in DI water for several times to remove the KOH remnants. To transfer the patterned film, the sapphire substrate with MoS<sub>2</sub> film is first covered with a polystyrene film by spin coating a solution of polystyrene in toluene onto the substrate, which is then immersed in DI water. To facilitate the lift-off process, a solution of KOH in DI water is also added for a short time. After that, the carrier polystyrene film with MoS<sub>2</sub> film is rinsed for several times in DI water. To remove the absorbed water the

polymeric film is dried at 50°C in dry air atmosphere and then transferred onto the paper. To improve the adhesion between the carrier polymer film and the wafer the sample is baked at 150°C for about an hour. The polystyrene carrier film is then dissolved in toluene resulting in MoS<sub>2</sub> film on the paper. Raman characterization before and after transfer has been performed with a Renishaw InVia spectrometer equipped with a confocal optical microscope and a 532 nm excitation laser. The spectral resolution of the system is 1 cm<sup>-1</sup>. Raman experiments were carried out employing a 50X objective (N.A. 0.6), laser power of 5 mW and an acquisition time of 2 s. The pixel size is 1 μm x 1 μm.

### **Devices fabrication**

MoS<sub>2</sub> transistors are fabricated in a top-gate/top-contact configuration on the CVD MoS<sub>2</sub> stripes transferred on paper. A Dimatix Materials Printer 2850 (Fujifilm) is used to define the contacts and the insulator layers under ambient conditions. The silver ink is deposited with a single printed pass using one nozzle, a drop spacing of 40 μm, and keeping the printer platen at room temperature. Cartridges with a typical droplet volume of 1 pL are used for the definition of the contacts. When the 2.5 mg ml<sup>-1</sup> graphene ink is employed, source and drain contacts are inkjet-printed by a drop spacing of 20 μm, and 20 printing passes. For the top gate contacts, only 6 printing passes of graphene ink at the same concentration are used in order to reduce the possibility of overlapping with the source and drain contacts (which would significantly increase the leakage current) at each print pass. A ~2 mg/mL hBN ink is printed on top of the CVD-grown layer using a drop spacing of 20 μm and 80 printing passes. No annealing is performed after the deposition of the insulator. Several transistors have been fabricated (with a yield of around 80%) and characterized with a nominal width of ~ 500 μm and length varying between 40 μm and 100 μm.



Parallel plate capacitors with silver/graphene bottom/top electrodes are also printed on paper to evaluate the capacitance of the hBN layers. The inks and the fabrication procedures are kept the same for all the reported devices.

### **Electrical characterization**

All the electrical measurements are performed in ambient conditions. The transistor characterization is carried out using a Keithley SCS4200 parameter analyzer. Capacitance measurements are performed with an R&S<sup>®</sup>RTO2014 oscilloscope and a HP 33120A function/arbitrary waveform generator. The detailed description of the measurement setup can be found in the *Supplementary information*.

### **Acknowledgements**

We acknowledge the ERC PEP2D (contract no. 770047) and H2020 WASP (contract no. 825213) for financial support. G.F., C.Co., T.M. acknowledges the Graphene Flagship Core2 (contract no. 785219). RW acknowledges the Hewlett-Packard Company for financial support in the framework of the Graphene NOWNANO Centre for Doctoral Training; C.Ca. acknowledges useful discussions with Alessandro Molle, and financial support from the Grand Challenge EPSRC grant EP/N010345/1.

### **Author Contributions**

R.W., S.M., developed the inks under the supervision of C.Ca.; D.K.P., M.P., S.P., D.H.K., and F.F. carried out the MoS<sub>2</sub> growth and the transfer on the paper substrates, and performed the Raman spectroscopy and imaging under the supervision of T.M and C.Co.; S.C., L.P., G.C., and G.F. fabricated the electronic devices, performed the electrical measurements, and analyzed the results; G.F, G.I., and M.M. designed and supervised the research. All authors discussed the results and contributed to the manuscript.

## References

1. Huang, S., Liu, Y., Zhao, Y., Ren, Z. & Guo, C. F. Flexible Electronics: Stretchable Electrodes and Their Future. *Adv. Funct. Mater.* **29**, 1805924 (2019).
2. Wang, C. *et al.* Advanced Carbon for Flexible and Wearable Electronics. *Adv. Mater.* **31**, 1801072 (2019).
3. Tobjörk, D. & Österbacka, R. Paper Electronics. *Adv. Mater.* **23**, 1935–1961 (2011).
4. Akinwande, D., Petrone, N. & Hone, J. Two-dimensional flexible nanoelectronics. *Nat. Commun.* **5**, 5678 (2014).
5. Franklin, A. D. Nanomaterials in transistors: From high-performance to thin-film applications. *Science (80-. )*. **349**, aab2750–aab2750 (2015).
6. Hernandez, Y. *et al.* High-yield production of graphene by liquid-phase exfoliation of graphite. *Nat. Nanotechnol.* **3**, 563–568 (2008).
7. Torrisi, F. *et al.* Inkjet-Printed Graphene Electronics. *ACS Nano* **6**, 2992–3006 (2012).
8. Finn, D. J. *et al.* Inkjet deposition of liquid-exfoliated graphene and MoS<sub>2</sub> nanosheets for printed device applications. *J. Mater. Chem. C* **2**, 925–932 (2014).
9. Carey, T. *et al.* Fully inkjet-printed two-dimensional material field-effect heterojunctions for wearable and textile electronics. *Nat. Commun.* **8**, 1202 (2017).
10. McManus, D. *et al.* Water-based and biocompatible 2D crystal inks for all-inkjet-printed heterostructures. *Nat. Nanotechnol.* **12**, 343–350 (2017).
11. Hu, G. *et al.* Functional inks and printing of two-dimensional materials. *Chem. Soc. Rev.* **47**, 3265–3300 (2018).
12. Manzeli, S., Ovchinnikov, D., Pasquier, D., Yazyev, O. V. & Kis, A. 2D transition metal dichalcogenides. *Nat. Rev. Mater.* **2**, 17033 (2017).
13. Kelly, A. G. *et al.* All-printed thin-film transistors from networks of liquid-exfoliated nanosheets. *Science (80-. )*. **356**, 69–73 (2017).

14. Kelly, A. G., Vega-Mayoral, V., Boland, J. B. & Coleman, J. N. Whiskey-phase exfoliation: exfoliation and printing of nanosheets using Irish whiskey. *2D Mater.* **6**, 045036 (2019).
15. Radisavljevic, B., Radenovic, A., Brivio, J., Giacometti, V. & Kis, A. Single-layer MoS<sub>2</sub> transistors. *Nat. Nanotechnol.* **6**, 147–150 (2011).
16. Li, J., Naiini, M. M., Vaziri, S., Lemme, M. C. & Östling, M. Inkjet Printing of MoS<sub>2</sub>. *Adv. Funct. Mater.* **24**, 6524–6531 (2014).
17. Tong, X., Ashalley, E., Lin, F., Li, H. & Wang, Z. M. Advances in MoS<sub>2</sub>-Based Field Effect Transistors (FETs). *Nano-Micro Lett.* **7**, 203–218 (2015).
18. Park, S. & Akinwande, D. First demonstration of high performance 2D monolayer transistors on paper substrates. *2017 IEEE International Electron Devices Meeting (IEDM) 5.2.1-5.2.4* (IEEE, 2017).
19. Lin, Z. *et al.* Solution-processable 2D semiconductors for high-performance large-area electronics. *Nature* **562**, 254–258 (2018).
20. Sahatiya, P. & Badhulika, S. Wireless, Smart, Human Motion Monitoring Using Solution Processed Fabrication of Graphene-MoS<sub>2</sub> Transistors on Paper. *Adv. Electron. Mater.* **4**, 1700388 (2018).
21. Xu, X. *et al.* High-Performance Monolayer MoS<sub>2</sub> Films at the Wafer Scale by Two-Step Growth. *Adv. Funct. Mater.* **29**, 1901070 (2019).
22. Rice, C. *et al.* Raman-scattering measurements and first-principles calculations of strain-induced phonon shifts in monolayer MoS<sub>2</sub>. *Phys. Rev. B* **87**, 081307 (2013).
23. Singh, M., Haverinen, H. M., Dhagat, P. & Jabbour, G. E. Inkjet Printing-Process and Its Applications. *Adv. Mater.* **22**, 673–685 (2010).
24. Worsley, R. *et al.* All-2D Material Inkjet-Printed Capacitors: Toward Fully Printed Integrated Circuits. *ACS Nano* **13**, 54–60 (2019).

25. Lu, S. *et al.* Flexible, Print-in-Place 1D–2D Thin-Film Transistors Using Aerosol Jet Printing. *ACS Nano* acsnano.9b04337 (2019).
26. Kim, T.-Y. *et al.* Electrical Properties of Synthesized Large-Area MoS<sub>2</sub> Field-Effect Transistors Fabricated with Inkjet-Printed Contacts. *ACS Nano* **10**, 2819–2826 (2016).
27. Zschieschang, U. & Klauk, H. Organic transistors on paper: a brief review. *J. Mater. Chem. C* **7**, 5522–5533 (2019).
28. Almora, O. *et al.* Capacitive Dark Currents, Hysteresis, and Electrode Polarization in Lead Halide Perovskite Solar Cells. *J. Phys. Chem. Lett.* **6**, 1645–1652 (2015).
29. Kong, D. *et al.* Capacitance Characterization of Elastomeric Dielectrics for Applications in Intrinsically Stretchable Thin Film Transistors. *Adv. Funct. Mater.* **26**, 4680–4686 (2016).
30. Dutta, K., Hazra, A. & Bhattacharyya, P. Ti/TiO<sub>2</sub> Nanotube Array/Ti Capacitive Device for Non-polar Aromatic Hydrocarbon Detection. *IEEE Trans. Device Mater. Reliab.* **16**, 235–242 (2016).
31. Zheng, J. *et al.* High-Mobility Multilayered MoS<sub>2</sub> Flakes with Low Contact Resistance Grown by Chemical Vapor Deposition. *Adv. Mater.* **29**, 1604540 (2017).
32. Wachter, S., Polyushkin, D. K., Bethge, O. & Mueller, T. A microprocessor based on a two-dimensional semiconductor. *Nat. Commun.* **8**, 14948 (2017).
33. Gao, Q. *et al.* Scalable high performance radio frequency electronics based on large domain bilayer MoS<sub>2</sub>. *Nat. Commun.* **9**, 4778 (2018).
34. Huang, J. *et al.* Highly Transparent and Flexible Nanopaper Transistors. *ACS Nano* **7**, 2106–2113 (2013).
35. Minari, T. *et al.* Room-temperature printing of organic thin-film transistors with  $\pi$ -junction gold nanoparticles. *Adv. Funct. Mater.* **24**, 4886–4892 (2014).
36. Fujisaki, Y. *et al.* Transparent Nanopaper-Based Flexible Organic Thin-Film

- Transistor Array. *Adv. Funct. Mater.* **24**, 1657–1663 (2014).
37. Hyun, W. J. *et al.* All-Printed, Foldable Organic Thin-Film Transistors on Glassine Paper. *Adv. Mater.* **27**, 7058–7064 (2015).
  38. Dai, S. *et al.* Intrinsically ionic conductive cellulose nanopapers applied as all solid dielectrics for low voltage organic transistors. *Nat. Commun.* **9**, 2737 (2018).
  39. Kraft, U. *et al.* Low-Voltage, High-Frequency Organic Transistors and Unipolar and Complementary Ring Oscillators on Paper. *Adv. Electron. Mater.* **5**, 1800453 (2019).
  40. Martins, R. F. P. *et al.* Recyclable, Flexible, Low-Power Oxide Electronics. *Adv. Funct. Mater.* **23**, 2153–2161 (2013).
  41. Thiemann, S. *et al.* Cellulose-based ionogels for paper electronics. *Adv. Funct. Mater.* **24**, 625–634 (2014).
  42. Kim, S. J. *et al.* Nonvolatile memory thin-film transistors using biodegradable chicken albumen gate insulator and oxide semiconductor channel on eco-friendly paper substrate. *ACS Appl. Mater. Interfaces* **7**, 4869–4874 (2015).
  43. Gaspar, D. *et al.* Planar Dual-Gate Paper/Oxide Field Effect Transistors as Universal Logic Gates. *Adv. Electron. Mater.* **4**, 1800423 (2018).
  44. Wang, X., Gao, Y., Liu, Z., Luo, J. & Wan, Q. Flexible Low-Voltage IGZO Thin-Film Transistors With Polymer Electret Gate Dielectrics on Paper Substrates. *IEEE Electron Device Lett.* **40**, 224–227 (2019).
  45. Liu, N., Yun, K. N., Yu, H.-Y., Shim, J. H. & Lee, C. J. High-performance carbon nanotube thin-film transistors on flexible paper substrates. *Appl. Phys. Lett.* **106**, 103106 (2015).
  46. Yoon, J. *et al.* Flammable carbon nanotube transistors on a nitrocellulose paper substrate for transient electronics. *Nano Res.* **10**, 87–96 (2017).
  47. Yoon, J. *et al.* Highly Flexible and Transparent Multilayer MoS<sub>2</sub> Transistors with

- Graphene Electrodes. *Small* **9**, (2013).
48. Lan, Y.-W. *et al.* Scalable fabrication of a complementary logic inverter based on MoS<sub>2</sub> fin-shaped field effect transistors. *Nanoscale Horizons* **4**, 683–688 (2019).
  49. Razavi, B. Design of Analog CMOS Integrated Circuits. 704 (2005).
  50. Wang, Z. *et al.* Current Mirror Array: A Novel Circuit Topology for Combining Physical Unclonable Function and Machine Learning. *IEEE Trans. Circuits Syst. I Regul. Pap.* **65**, 1314–1326 (2018).
  51. Coleman, J. N. *et al.* Two-Dimensional Nanosheets Produced by Liquid Exfoliation of Layered Materials. *Science (80-. )*. **331**, 568–571 (2011).
  52. Dumcenco, D. *et al.* Large-Area Epitaxial Monolayer MoS<sub>2</sub>. *ACS Nano* **9**, 4611–4620 (2015).
  53. Gurarlan, A. *et al.* Surface-Energy-Assisted Perfect Transfer of Centimeter-Scale Monolayer and Few-Layer MoS<sub>2</sub> Films onto Arbitrary Substrates. *ACS Nano* **8**, 11522–11528 (2014).

Supplementary information for

***Low-voltage 2D materials-based printed field-effect transistors for integrated digital and analog electronics on paper***

*Silvia Conti, Lorenzo Pimpolari, Gabriele Calabrese, Robyn Worsley, Subimal Majee, Dmitry K. Polyushkin, Matthias Paur, Simona Pace, Dong Hoon Keum, Filippo Fabbri, Giuseppe Iannaccone, Massimo Macucci, Camilla Coletti, Thomas Mueller, Cinzia Casiraghi, Gianluca Fiori*

**S1. Capacitance measurement**

The measurements of the insulator capacitance are carried out using parallel plate capacitor structures, as described in the main text. In order to measure the capacitance at low frequency (i.e. in quasi-static conditions), the circuit shown in Figure S1a is used.

The capacitor under test,  $C$ , forms a capacitive voltage divider with a commercial test capacitor,  $C_T$ , with known value on the non-inverting input of an operational amplifier (Op-Amp). The Op-Amp is connected in non-inverting configuration, and has a voltage gain:

$$A_V = 1 + \frac{R_2}{R_1} \quad (1)$$

where  $R_1$  and  $R_2$  are two resistances, chosen to have a voltage gain of 4, in order to properly amplify the input signal. The waveform generator provides a low frequency (down to 5 mHz) sine wave  $V_{in}$ , that is applied to an input of the oscilloscope and to the capacitor under test. The voltage at the Op-Amp input, given by:

$$V^+ = V_{in} \frac{C}{C+C_T} \quad (2),$$

is amplified to obtain the output voltage  $V_{out} = A_V V^+$ ; this voltage is sent to an input of the oscilloscope. However, it is necessary to take into account that  $C$  is not an ideal capacitor; in order to have a more realistic model, the capacitor is represented with the equivalent circuit shown in Figure S1b, according to <sup>1</sup>  $C_p$  represents the capacitive part of the capacitor, while the resistor  $R_p$  takes into account the dielectric leakage. Therefore, the output voltage is modified as follows:

$$V_{out} = A_V \frac{R_p C_p s + 1}{R_p (C_T + C_p) s + 1} V_{in} = H(s) V_{in} \quad (3)$$

where  $s$  is the Laplace generalized frequency and  $H(s)$  is the transfer function between  $V_{in}$  and  $V_{out}$ . Figure S1c shows the voltages  $V_{in}$  and  $V_{out}$  measured with the oscilloscope. The phase shift  $\varphi_0$  between the two sine waves, highlighted in Figure S1d, is due to the presence of the resistance  $R_p$ .

The measurement of the output voltage amplitude and the phase shift  $\varphi_0$ , i.e. of the module and phase of the transfer function  $H(f)$  ( $f$  is the frequency), allows to solve the system of non-linear equations:

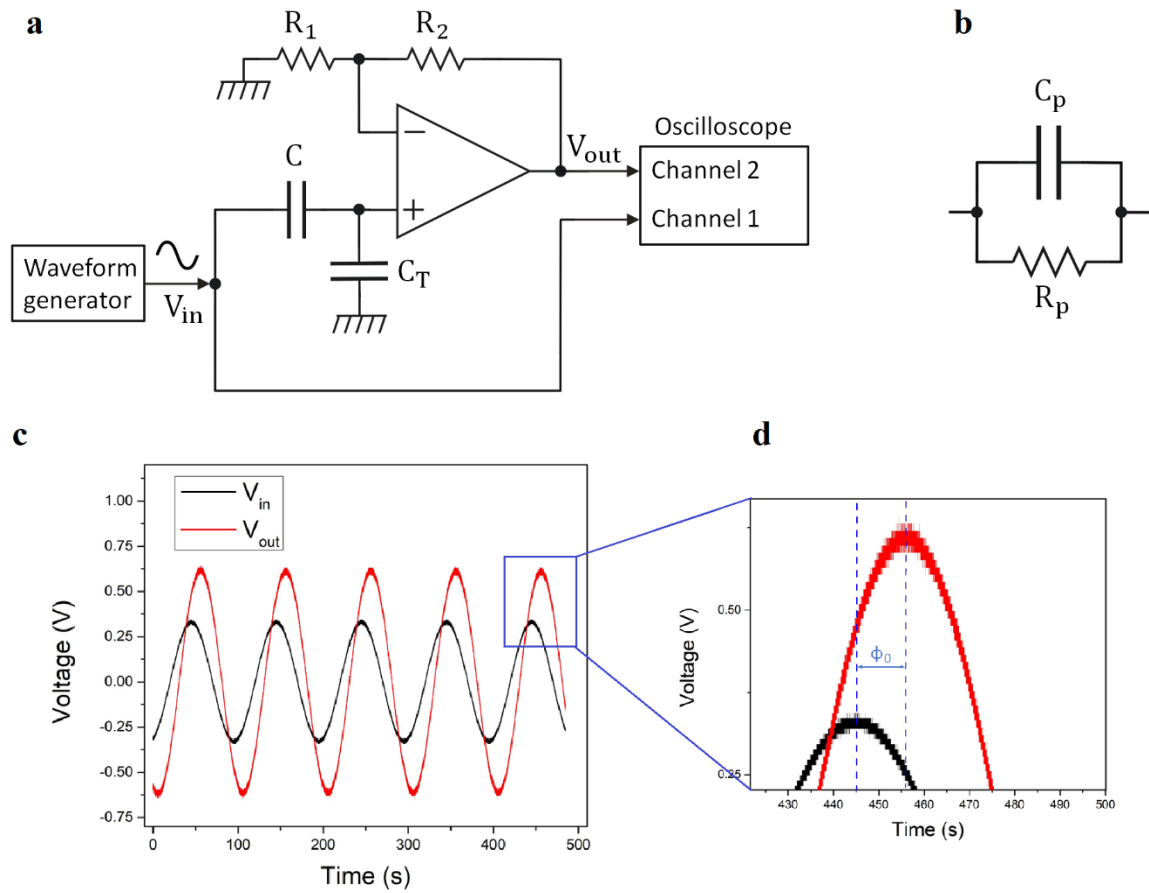
$$\begin{cases} |H(f)| = \frac{\sqrt{R_p^2 C_p^2 (2\pi f)^2 + 1}}{\sqrt{R_p^2 (C_T + C_p)^2 (2\pi f)^2 + 1}} \\ \angle H(f) = \text{atan}(R_p C_p 2\pi f) - \text{atan}(R_p (C_T + C_p) 2\pi f) \end{cases} \quad (4)$$

and, therefore, to obtain the resistance  $R_p$  and the capacitance  $C_p$ . The insulator areal capacitance is obtained dividing the extracted capacitance value by the area of the test capacitor.

The extracted average value of 230 nF/cm<sup>2</sup> explains the low threshold voltages of the devices. In quasi-static conditions, the presence of both water molecules (water is the solvent of the hBN ink employed in this work <sup>2</sup>) and impurities (moisture absorbance, mobile ions) in the



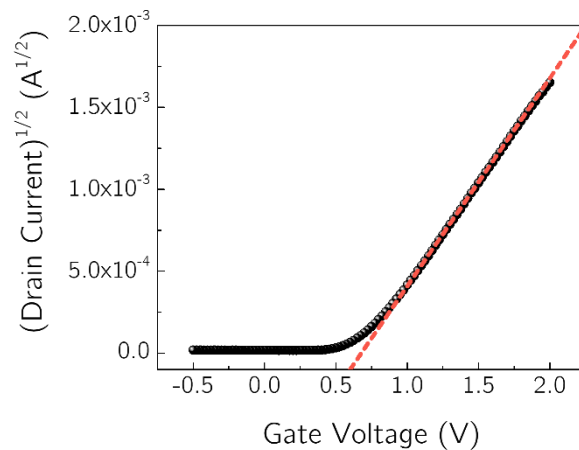
films could influence the charging processes thus increasing its permittivity, as widely observed for both organic and hybrid materials<sup>3,4,5,6,7</sup>.



**Figure S1 | Capacitance measurement setup.** **a**, schematic of the electronic circuit used for the measurement of the capacitance. **b**, Equivalent circuit of the capacitor under measurement. **c**, Input and output voltages as a function of time. **d**, magnification of the measured signals showing the phase shift between the input and output voltages.

## S2. Detailed electrical characterization

The values of threshold voltage and field-effect mobility reported in the main text are evaluated using the following procedures. Figure S2 shows the square root of the channel current as a function of the gate voltage for a representative device. The value of threshold voltage is extrapolated as the  $x$  axis intercept of the straight line fitting the square root of the drain current, as shown in the figure. The field-effect mobility has been extracted using the formula in saturation regime [equation (1) in the main text].



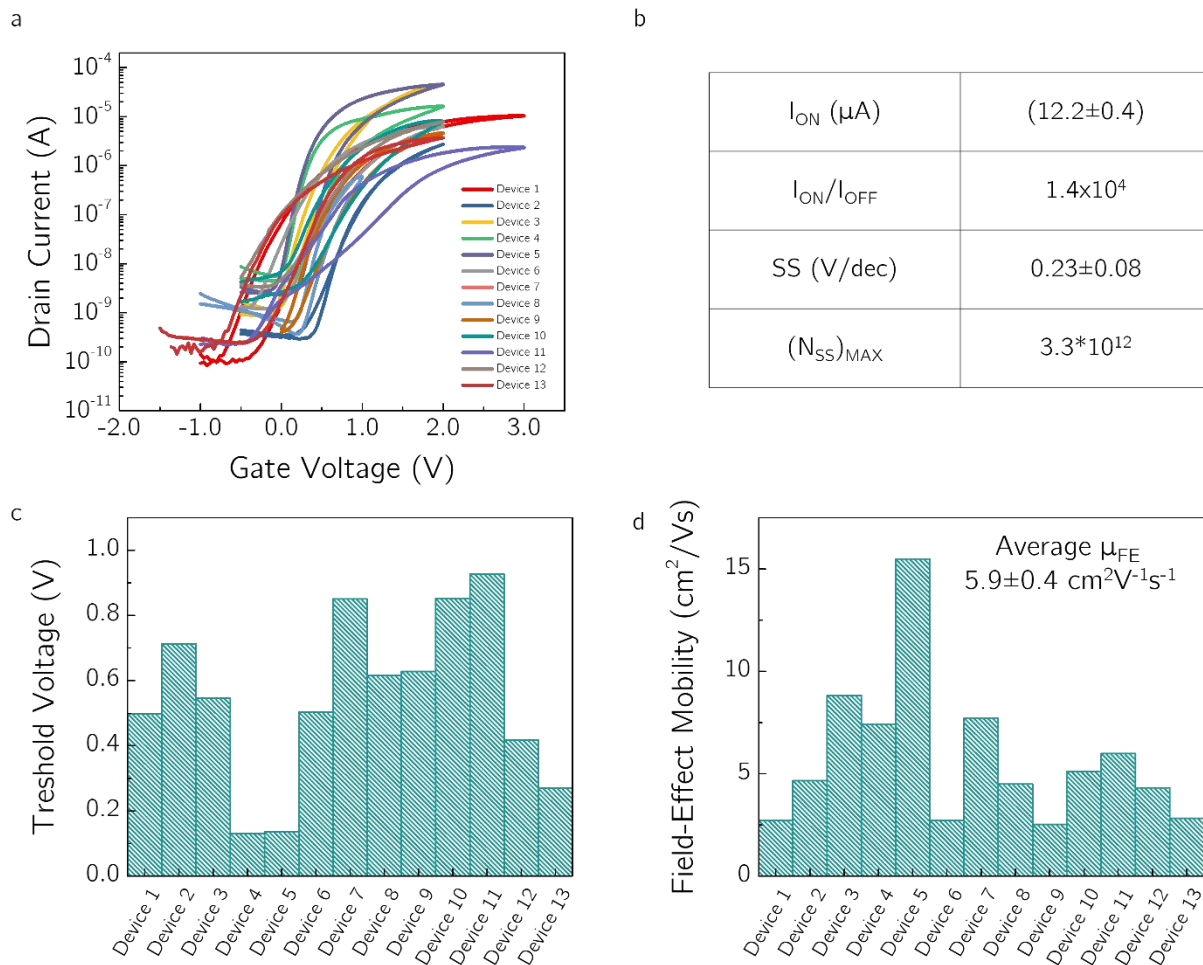
**Figure S2 | Extraction of the MoS<sub>2</sub> FET electrical parameters.** Square root of the drain current as a function of the gate voltage. Fit line in red illustrates the range used to fit the data and extract the threshold voltage and the field-effect mobility value.

Figure S3a shows the transfer characteristics for 13 devices. The  $I_{ON}$  current varies from 1  $\mu$ A to 50  $\mu$ A; this variation could be attributed to the non-homogeneity in the CVD MoS<sub>2</sub> and to the different channel dimensions in the investigated devices. The average  $I_{ON}$  is shown in Figure S3b together with the average  $I_{ON}/I_{OFF}$  ratio, subthreshold slope ( $SS$ ), and maximum surface trap density values ( $N_{SSmax}$ ). A  $SS$  in the range of 200 mV/dec has been measured and a  $N_{SSmax}$  of the order of  $10^{12}$  cm<sup>-2</sup> has been calculated from the relationship<sup>8</sup>:

$$N_{SSmax} = \left( \frac{SS * \log e}{q/KT} - 1 \right) \frac{C_i}{q} \quad (5)$$

where  $K$  is the Boltzmann constant,  $q$  is the elementary charge, and  $T$  is the temperature.

The values of the threshold voltage and the field-effect mobility of each device are reported in the column charts of Figure S3c and Figure S3d, respectively.



**Figure S3 | Electrical parameters of 13 MoS<sub>2</sub> FETs. a,** Transfer characteristic curves. **b,** Average electrical key parameters. **c,** Column chart showing the treshold voltage values **d,** Column chart showing the field-effect mobility values.

### S3. Literature table for Figure 2e

**Table S1** | Literature table showing the reference number, materials and deposition techniques, power supply,  $\mu_{FE}$ , and  $I_{ON}/I_{OFF}$  for the manuscripts reported in Figure 2e of the main text. The reference numbers are the ones from the main text. The power supply (i.e., the range of the applied gate voltage) is classified as high voltage (HV, above 10 V) or low voltage (LV, below 10 V). G, gate electrode; S/D, source/drain electrode; where not specified the same material is used for all the electrodes.

Reference	Semiconductor/ deposition technique	Insulator/ deposition technique	Contacts/ deposition technique	Power supply	$\mu_{FE}$ [cm <sup>2</sup> /Vs]	$I_{ON}/I_{OFF}$
34	NTCDI-F15/ Vacuum deposition	PMMA/ Spin coating	SWCNTs (G)/ Meyer Rod coating	HV	5x10 <sup>-3</sup>	2x10 <sup>2</sup>
			Silver (S/D)/ Thermal evaporation			
35	C <sub>8</sub> -BTBT/ Screen printing and solution casting	Cytop/ Spin coating	Au NPs/ Selective deposition	HV	2.5	10 <sup>6</sup>
36	LisiconS1200/ Spin coating	Fluoro-based polymer/ Spin coating	Mo (G)/ Sputtering	HV	1.3	10 <sup>7</sup>
			Au (S/D) e-beam deposition			
37	P3HT/ Aerosol-jet printing	Ion gel/ Custom-built Inkjet printing	Graphene/ Screen printing	LV	0.14	3x10 <sup>3</sup>
38	C <sub>8</sub> -BTBT/ Thermal evaporation	ICCN/paper	Au/ Thermal evaporation	LV	0.07	7x10 <sup>3</sup>
39	DNTT/ Sublimation in vacuum	AlO <sub>x</sub> /SAM Plasma treatment	Al/ Thermal evaporation	LV	1.1	1x10 <sup>7</sup>
40	IGZO/ Sputtering	paper	IZO (G)/ Sputtering	HV	22	2x10 <sup>5</sup>
			Ni/Au (S/D)/ e-beam evaporation			

41	ZnO-NRs/ Drop casting	Cellulose- Ionogel/ Lamination	Au/ e-beam evaporation	LV	0.03	10 <sup>2</sup>
42	IGZO	Chicken albumen/ Spin coating	ITO (S/D)/ Magnetron sputtering	HV	11	10 <sup>6</sup>
			Al (G/S/D)/ Thermal evaporation			
43	IGZO/ Magnetron sputtering	paper	Al (G/S/D)/ e-beam evaporation	HV	3	10 <sup>4</sup>
			IZO (G)/ Magnetron sputtering			
44	IGZO/ Magnetron sputtering	PVA/ Spin coating	Ag/ Thermal evaporation	LV	42	10 <sup>7</sup>
45	SWCNTs/ Dip-coating	Al <sub>2</sub> O <sub>3</sub> / Atomic layer deposition	Ti/Au (S/D)/ e-beam evaporation	HV	3	6x10 <sup>5</sup>
46	CNTs/ Dip-coating	Al <sub>2</sub> O <sub>3</sub> / Atomic layer deposition	Ti/Pd Thermal evaporation	LV	4	10 <sup>3</sup>
18	MoS <sub>2</sub> / CVD	Al <sub>2</sub> O <sub>3</sub> / Atomic layer deposition	Cr/Al (G) e-beam evaporation	LV	6	10 <sup>6</sup>
			Ni/Au (S/D)/ e-beam evaporation			
20	Graphene/MoS <sub>2</sub> Dip Coating	paper	Graphite/ Drawing	HV	18.7	10 <sup>2</sup>

## **S4. CVD grown MoS<sub>2</sub> on SiO<sub>2</sub>/Si substrate**

### **S4.1 Growth and transfer**

As an alternative to sapphire, we have considered the CVD growth of MoS<sub>2</sub> on top of SiO<sub>2</sub> substrates. In particular, the MoS<sub>2</sub> flakes were obtained using the liquid precursor CVD (LPCVD) growth method<sup>9</sup>. First, two aqueous solutions (solution A and solution B) containing ammonium heptamolybdate (AHM, SigmaAldrich, 431346), as Mo precursor, and NaOH, as growth promoter, were prepared by dissolving 0.4 g of AHM in 30 ml deionized (DI) water and 0.1 g of NaOH in 40 ml of DI water, respectively. Then, solution A, solution B and iodixanol (Sigma-Aldrich, Opti Prep, D1556) were mixed using a ratio of 1 : 1.5 : 1 and spin coated on Si/SiO<sub>2</sub> substrate, which was previously cleaned in acetone, isopropanol and treated with oxygen plasma for 5 minutes. The growth was carried out in a two-zone horizontal furnace, where the spin coated substrate was heated at 700 °C in atmospheric pressure for 15 minutes under constant Ar flux, while sulphur was maintained at 200 °C. After growth, the MoS<sub>2</sub> flakes were transferred on paper using a semi-dry transfer approach as reported in<sup>10</sup>. Specifically, the sample was covered by a polymeric membrane of PMMA baked at 90 °C for 2 minutes. Then, the sample was covered using a PDMS frame and left in water at 60 °C until complete detachment of the membrane. After detachment, the free-standing membrane was transferred on the ceramic paper using a transfer set up, as previously reported<sup>11</sup>. Finally, the transferred sample was cleaned in acetone overnight until complete removal of PMMA.

### **S4.2 Characterization of MoS<sub>2</sub> monolayers before and after transfer**

The secondary electron (SE) imaging of the MoS<sub>2</sub> monolayers (MLs), before the transfer process, was carried out in a Zeiss Merlin SEM with an accelerating voltage of 5 kV.

Scanning Raman spectroscopy was performed with a Renishaw InVia spectrometer equipped with a confocal optical microscope and a 532 nm excitation laser. The spectral resolution of the system is 1 cm<sup>-1</sup>. Raman experiments were carried out employing a 50X objective (N.A. 0.6), laser power of 5 mW and an acquisition time of 2 s. The pixel size is 1 μm x 1 μm.

The Raman map of the separation of the  $E_{2g}$  and  $A_{1g}$  modes, reported in Figure S4, indicates a highly homogenous monolayer  $\text{MoS}_2$  crystal. It is worth noting that the black spots with a separation higher than  $21 \text{ cm}^{-1}$  can be related to bilayer terraces.

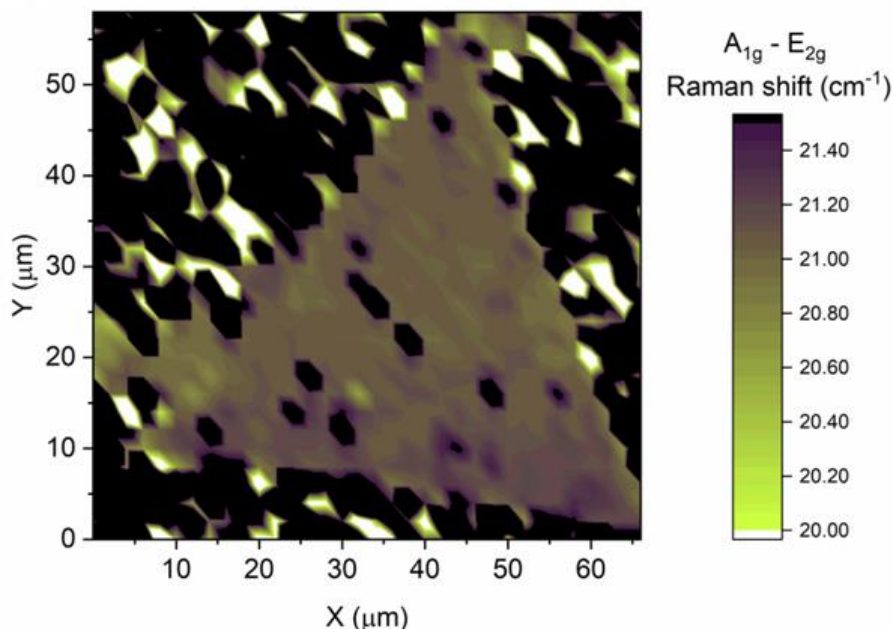


**Figure S4 | Raman map showing the separation of the  $E_{2g}$  and  $A_{1g}$  Raman modes.**

Figure S5 shows the Raman maps of  $A_{1g} / E_{2g}$  intensity ratio modes  $\text{MoS}_2$  ML on the growth substrate (a) and on paper after transfer (b). The statistical analysis, reported in Figure S5c highlights the increases of the  $A_{1g} / E_{2g}$  intensity ratio, suggesting an increase of sulphur vacancies concentration in the  $\text{MoS}_2$  ML after the transfer process.

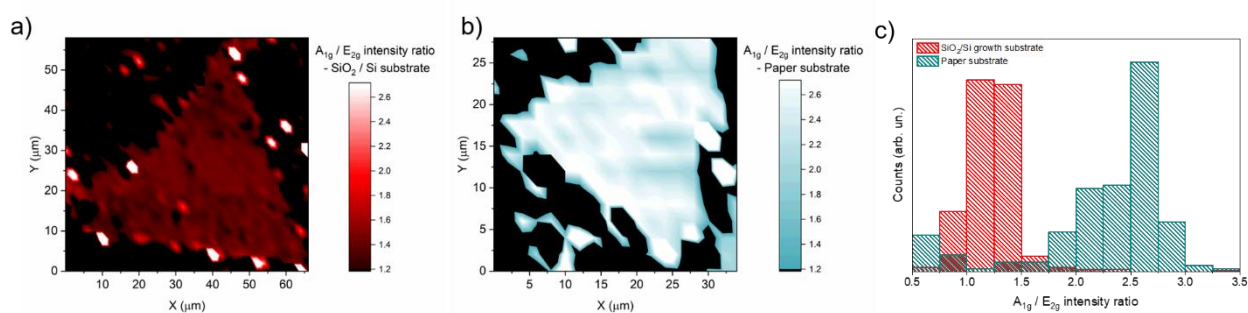


**Figure S5 | a,** Raman map showing the  $A_{1g}/E_{2g}$  ratio of  $\text{MoS}_2$  flake on the growth substrate. **b,** Raman map showing the  $A_{1g}/E_{2g}$  ratio of  $\text{MoS}_2$  flake on paper after transfer. **c,** Statistical analysis of the  $A_{1g} / E_{2g}$  ratio before and after the transfer.

### S4.3 Electrical Characterization

Figure S6a shows a single flake of MoS<sub>2</sub>, which constitutes the device channel, in between the inkjet-printed silver source and drain contacts. The purple dotted line highlights the edges of the flake. Figure S6b shows the complete device after printing the hBN dielectric film and the silver gate contact. The inks and the fabrication procedures for all the different components are the same as the reported in the main text (see *Methods*). A representative transfer characteristic curve is shown in Figure S6c. Considering that the channel width of this transistor ( $W \approx 50 \mu\text{m}$ ) is significantly smaller than that of the device shown in Figure 2a, b, c, d, the current densities (i.e.  $I_{DS}/W$ ) of the two devices are comparable. However, several non-idealities can be observed as, for example, a quite high  $I_{OFF}$  current. The threshold voltage is slightly negative in this case (around -1.1 V), i.e. the transistor works in depletion mode. Moreover, the mobility calculated for this transistor ( $0.5 \text{ cm}^2/\text{Vs}$ ) is smaller than the ones extracted for the other devices (see Figure S3d) based on MoS<sub>2</sub> grown on sapphire substrate, on which the results of the main text are based on. This could be probably due to the presence of sulfur vacancies, detrimental for the transport, as highlighted through the Raman analysis.



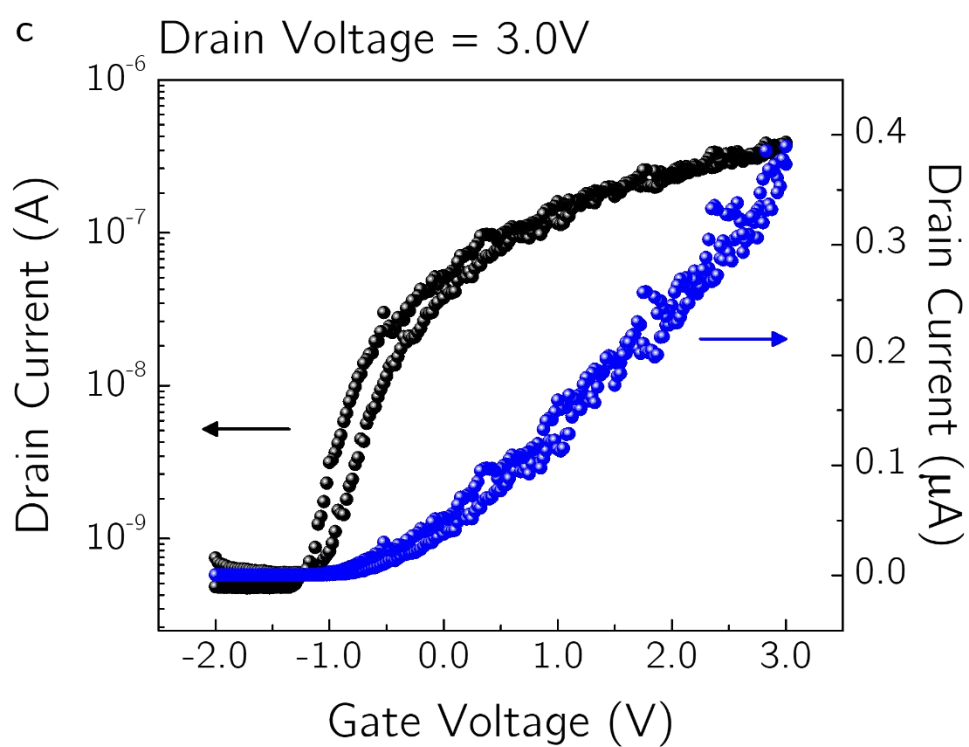
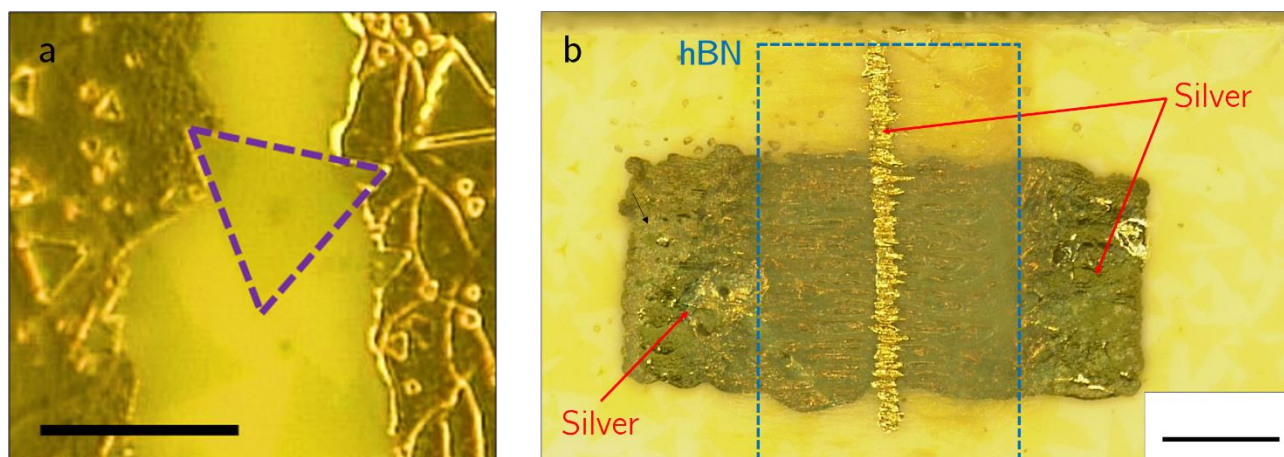


**Figure S6 | Device based on single-layer CVD grown MoS<sub>2</sub>.** **a**, Optical image of single flake of MoS<sub>2</sub> in between silver contacts. The scale bar corresponds to 50 μm. **b**, optical micrograph of the final device, after printing the hBN dielectric film and the silver gate contact. The scale bar corresponds to 250 μm. **c**, Typical transfer characteristic of a transistor based on single-layer MoS<sub>2</sub>.

## References

1. Worsley, R. *et al.* All-2D Material Inkjet-Printed Capacitors: Toward Fully Printed Integrated Circuits. *ACS Nano* **13**, 54–60 (2019).
2. McManus, D. *et al.* Water-based and biocompatible 2D crystal inks for all-inkjet-printed heterostructures. *Nat. Nanotechnol.* **12**, 343–350 (2017).
3. Bäcklund, T. G., Österbacka, R., Stubb, H., Bobacka, J. & Ivaska, A. Operating principle of polymer insulator organic thin-film transistors exposed to moisture. *J. Appl. Phys.* **98**, 074504 (2005).
4. Kim, S. H. *et al.* Effect of the hydrophobicity and thickness of polymer gate dielectrics on the hysteresis behavior of pentacene-based field-effect transistors. *J. Appl. Phys.* **105**, (2009).
5. Kong, D. *et al.* Capacitance Characterization of Elastomeric Dielectrics for Applications in Intrinsically Stretchable Thin Film Transistors. *Adv. Funct. Mater.* **26**, 4680–4686 (2016).
6. Zhang, C. X. *et al.* Total ionizing dose effects on hBN encapsulated graphene devices. *IEEE Trans. Nucl. Sci.* **61**, 2868–2873 (2014).
7. Tsekmes, I. A., Kochetov, R., Morshuis, P. H. F. & Smit, J. J. Evaluating the effect of particle distribution and dispersion on the dielectric response of boron nitride - epoxy nanocomposites. in *2014 IEEE Electrical Insulation Conference (EIC)* 329–332 (IEEE, 2014). doi:10.1109/EIC.2014.6869403
8. Rolland, A. Electrical Properties of Amorphous Silicon Transistors and MIS-Devices: Comparative Study of Top Nitride and Bottom Nitride Configurations. *J. Electrochem. Soc.* **140**, 3679 (1993).
9. Kim, H. *et al.* Role of alkali metal promoter in enhancing lateral growth of monolayer transition metal dichalcogenides. *Nanotechnology* **28**, (2017).
10. Miseikis, V. *et al.* Deterministic patterned growth of high-mobility large-crystal graphene: A path towards wafer scale integration. *2D Mater.* **4**, (2017).
11. Miseikis, V. *et al.* Rapid CVD growth of millimetre-sized single crystal graphene using a cold-wall reactor. *2D Mater.* **2**, (2015).